Extreme Mechanics Letters 43 (2021) 101146

Contents lists available at ScienceDirect

Extreme Mechanics Letters

journal homepage: www.elsevier.com/locate/eml

Programmable 3D structures via Kirigami engineering and controlled stretching

Nicolas A. Alderete [a], Lior Medina [b], Luciano Lamberti [c], Cesar Sciammarella [d], Horacio D. Espinosa [a,b,*]

[a] Theoretical and Applied Mechanics Program, Northwestern University, Evanston, IL 60208, USA
[b] Department of Mechanical Engineering, Northwestern University, Evanston, IL 60208, USA
[c] Dipartimento di Meccanica, Matematica e Management, Politecnico di Bari, Bari 70125, Italy
[d] Department of Mechanical, Materials and Aerospace Engineering, Illinois Institute of Technology, Chicago, IL 60616, USA

ARTICLE INFO

Article history:
Received 13 October 2020
Received in revised form 7 December 2020
Accepted 9 December 2020
Available online 14 December 2020

Keywords:
Kirigami
Metamaterials
Bifurcations
3D morphing
Shadow Moiré

ABSTRACT

Kirigami with a variety of cut patterns have been recently investigated as means to transform 2D surfaces into 3D structures, offering a number of functionalities. In this work, we show that a single Kirigami motif, defining two inner panels connected by hinges, can generate a rich variety of out-of-plane symmetric and asymmetric deformation modes. The out-of-plane responses, caused by local instabilities when a far field tensile load is applied, manifest themselves at the inner plates, exhibiting a combination of one- and two-dimensional rotations (tilt and twist), effectively morphing the planar geometries into complex 3D surfaces. By conducting numerical analyses and experiments, the relationship between changes in the cut geometry, and out-of-plane responses is identified. In particular, two types of instabilities emerge, coincident bifurcation points for both inner plates, responsible for two-dimensional tilts, and sequential bifurcation points, which produce one-dimensional tilts with distinct buckling thresholds. Nonlinear parametric finite element analysis (FEA) is used to explore the space of possible configurations and characterize the behavior of the structure as a function of its parameters, revealing a variety of deformation modes and structural responses of interest. Numerical predictions are experimentally validated using paper Kirigami and the shadow Moiré technique. The combined numerical–experimental approach reveals a plethora of programmable and controllable deformation modes with intrinsic nonlinear behaviors, enabled by tunable imperfections, which promise to influence a variety of applications ranging from light modulation to fluid flow control.

1. Introduction

Kirigami, the age-old Japanese art form of paper cutting, has recently transcended its original artistic purpose to become an unequivocal pathway to the creation of complex structures and metastructures. From increased flexibility and stretchability in two-dimensional materials like MoS_2 and graphene [1,2], through out-of-plane morphability [3], to bistability [4,5], the value of Kirigami-based structures is rich and manifold. Remarkably, from a mechanistic viewpoint, these structures are able to exhibit out-of-plane deformations, elicited by buckling instabilities under tension [3,6], as opposed to compression induced buckling, which is traditionally observed in beams and plates [7]. Furthermore, recent developments have shown that such bifurcations can also yield symmetry breaking [8], hitherto known to primarily occur in bistable structures (e.g., curved beams, plates and shells) [9–11]. In sharp contrast to the conventional notion of buckling as a phenomenon to be avoided, the presence of instabilities can be exploited to engineer smart structures with broad applicability [12]; a distinction that has found its way to metamaterials, where Kirigami structures are particularly attractive candidates for controllable shape morphing applications [13].

Interestingly, the space of infinite geometric variations pertaining to a given Kirigami motif entails an equally vast space of possibilities to identify and harness unusual mechanical behaviors and programmable out-of-plane deformation modes. In an attempt to address this seemingly intractable design problem, a subset of geometric configurations, driven by asymmetries in hinges and cuts, are investigated based on the same Kirigami motif. Beyond cut design, we provide insights into the subject

* Correspondence to: Theoretical and Applied Mechanics Program, Northwestern University, 2145 Sheridan Rd., Evanston, IL 60208, USA. Department of Mechanical Engineering, Northwestern University, 2145 Sheridan Rd., Evanston, IL 60208, USA.

E-mail address: espinosa@northwestern.edu (H.D. Espinosa).

https://doi.org/10.1016/j.eml.2020.101146
2352-4316/

of imperfection control and their impact in Kirigami out-of-plane displacements, an essential and previously unaddressed question. Lastly, the present investigation attempts to further elucidate the merits of Kirigami structures, which have already spurred novel behaviors, and continue to open up new frontiers in the realization of applications such as sensitive tensile strain sensors [14], biomimetic robots [15,16], tunable diffraction gratings [17], and solar trackers [7,18].

2. Materials and methods

2.1. Modeling

Consider a flat plate comprised of an array of rectangular Kirigami unit cells, Fig. 1a. Each unit cell, Fig. 1b, is assumed to be initially flat and stress free, exhibiting a Kirigami motif of thin cuts, parallel to the x and y axes. One of the cuts, of width c_y and exhibiting a C-shape, is defined by lengths L_x and L_y. The other two cuts, of length L_h and width c_x, define hinges of length h on either side, Fig. 1c. These cuts delimit an inner plate with two interior panels connected by hinges. Dimensions e_x and e_y, describe distances from the loaded and unloaded edges, respectively, fully defining the unit cell. The plate is assumed to be made from a homogeneous, isotropic, linear elastic material with Young's modulus E and Poisson's ratio ν. It has thickness d, which is much smaller than the overall length and width of the structure. Based on these assumptions, the structure is modelled as a shell. Since an analytical formulation for this type of structure is currently unavailable, it was studied via geometric nonlinear FEA, using three-dimensional, finite strain, S4R shell elements [19], with an average size of $c_y/2$, based on prior convergence studies and experimental validations [8]. In line with the work carried out in [8], the elastic properties of the simulated Kirigami correspond to those of Si_3N_4. While a specific material must be considered in the FEA, the fact that the study deals with mechanical–structural phenomena in general and buckling in particular, entails material-independent results, provided that the loading is within the elastic regime [20,21].

With the objective of comprehensively exploring the space of possible three-dimensional shapes, elicited by specific variations of the generic Kirigami motif, analyses were conducted for five different general configurations. The first three configurations explored the effect of asymmetries in the length of the hinges (h) with respect to the x- and y-axes (x-asymmetric, y-asymmetric), as well as a combination of both asymmetries (xy-asymmetric). The remaining two configurations explored the influence of asymmetries in the lengths (L_h) and widths (c_x) of the cuts separating the hinges.

The general dimensions of the Kirigami layout and the material properties used in the numeric models are given in Table 1. The values of h, c_x and L_h, presented as constants in Table 1, represent the upper bounds of the explored parametric space. To trigger out-of-plane deformation in the structure, each FEA was preceded by a linear buckling analysis, from which the first asymmetrical eigenmode was extracted, scaled to a maximum amplitude of 1% with respect to the plate thickness, and used as an initial perturbation in the subsequent geometric nonlinear FEA [8]. In the latter, the imperfect structure was subject to a displacement of $\Delta x/d = 1$ along an edge, with the opposite edge fully clamped. Following each FEA run, the angular rotations θ_x and θ_y of the interior panel, closer to the origin, were extracted using the center node along the edge (marked as the red dot in Fig. 1b). Equilibrium curves were then generated from the reaction forces, divided by the nominal cross section.

Table 1
Geometric and material parameters considered for the FE models.

Dimension	Description
$d = 0.1$ mm	Thickness
$L_y = 3.5$ mm	Inner plate width
$L_x = 3.5$ mm	x-cut length
$c_y = 0.1$ mm	x-cut width
$L_h = 0.1$ mm	Hinge-cut length
$c_x = 0.1$ mm	Hinge-cut width
$h = 0.5$ mm	Hinge length
$e_x = 1$ mm	x-cut distance to the clamped edge
$e_y = 1.5$ mm	y-cut distance to the free edge
$E = 250$ GPa	Young's modulus
$\nu = 0.23$	Poisson's ratio

2.2. Tensile tests and shadow Moiré analysis

Experimental validation of a subset of the diverse shapes, predicted by the FEA, was pursued using white paper specimens (130 grams per square meter, 150–200 μm thick), with cuts manufactured using a ILS12.150D Laser Cutter (Universal Laser Systems GmbH, Power: 45 W). In particular, one case from each generic geometric configuration (e.g., asymmetrical hinges, asymmetrical cut lengths and widths) was selected for proof of concept. Since the behavior of any structure, particularly Kirigami-based ones, depend solely on the aspect ratio of normalized dimensions (e.g., by its thickness), it is possible to scale up the structures analyzed in the FEA, and attain the same responses [20,22]. Accordingly, parameters of the simulated Kirigami were uniformly scaled by a factor of 1.8 for ease of handling and visualization.

The nature of the instability-triggered deformations in flat Kirigami, consisting primarily of out-of-plane displacements (w), makes the classic technique of shadow Moiré (SM) ideally suited for shape characterization. In SM, a linear reference grating of pitch length p is held fixed before a surface of interest and light is used to illuminate the grating, thus projecting shadow fringes on the specimen. Upon out-of-plane deformation, the projected shadow grating and the reference grating interact to form Moiré Fringes (MF), from which the topography of the deformed object can be calculated. Under the assumption of rectilinear propagation of light, the depth between two consecutive MF becomes a function of the reference grating pitch (p), and both the angle of illumination (α) and observation (β), viz. [23,24]:

$$w = \frac{p}{\tan\alpha + \tan\beta} \tag{1}$$

To ensure constant sensitivity and reduce the deleterious gap effect [25], the optical setup is usually arranged so that the light source and the observer are at the same vertical distance L from the specimen, which reduces the denominator in Eq. (1) to a constant parameter $K = D/L$ [25,26]. Furthermore, normal observation (i.e., $\beta = 0$) is preferred to avoid distortions when viewing the specimen.

In accordance with the aforementioned, an SM setup was configured, as shown in Fig. 2. On the illumination leg, a 150 W optical fiber illuminator (AmScope, Series Haloid Lamp) was placed at a distance of $f = 250$ mm from a plano-convex lens used to collimate light, which was subsequently directed by a set of planar mirrors upon the specimen to attain a constant sensitivity of $K = 0.98$. Observation was performed at a normal angle by means of a Mako U-503B CCD Monochrome Camera (Allied Vision Technologies GmbH) with 5 Megapixel resolution, after passage through a 1x objective. The Kirigami samples were placed on a micro-mechanical testing platform (Ernest F. Fullam Inc.) with their edges glued, and commercial chrome on glass Ronchi Rulings of 100 line-pairs per inch (i.e., 100 lpi, $p = 0.254$ mm) placed at a distance of 2 mm before the specimens,

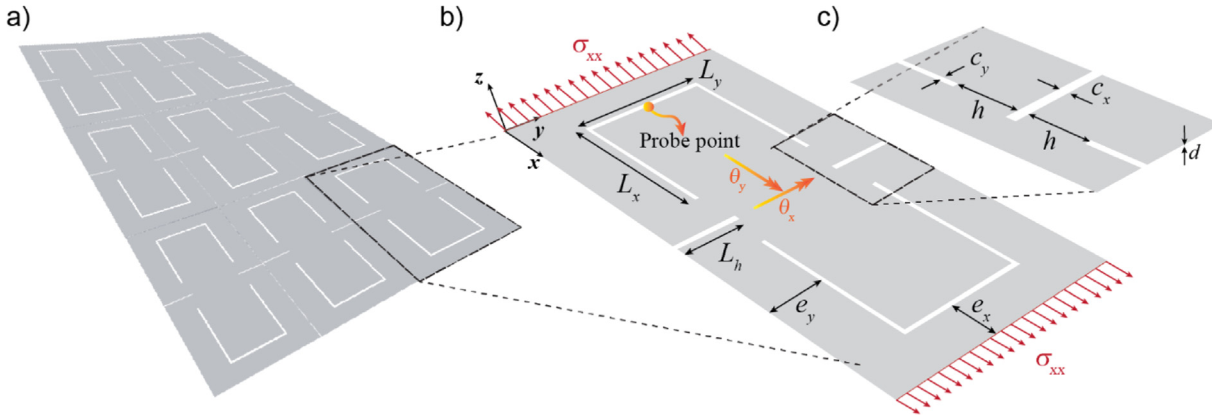

Fig. 1. Representative Kirigami motif. (a) A 2D array of Kirigami unit cells. (b) Schematic diagram of a single unit cell with thickness d, constituting a Kirigami based plate. The unit cell is externally actuated via an in-plane stress σ_{xx} (in red). An inner plate, comprised of two panels and separated from the main plate by cuts of width c_y (inset c), is defined by dimensions L_x, L_y, e_x and e_y, which are plate length and width, and distances from the loaded and unloaded edges, respectively. The panels are separated by two cuts of width c_x and length L_h, adjacent to two hinges of size h at either side, (inset c). Tilt angles, θ_x and θ_y, are represented by the orange double arrows. The orange circle marks the location at which the angles were extracted at the end of each FEA run.

were used as reference gratings (Edmund Optics), as depicted in Fig. 2(b). Tensile tests were conducted under displacement control, at constant quasi-static rates, and the resulting Moiré pattern recorded after stopping the test. In order to avoid loss of fringe contrast from the Talbot Effect [26], and plastic hinge deformation, Kirigami samples were not stretched beyond 500 μm.

Unlike the sister method of projection Moiré, in SM, recorded images naturally include the image of the reference grating, which must be removed prior to accessing the information contained in the MF, Fig. 2(c), (i). To that end, the enhanced images are first transformed to the frequency domain, via a Two-Dimensional Discrete Fast Fourier Transform, where the periodic nature of the reference grating adopts a natural representation in the form of bright orders along a principal frequency axis. Following suppression of the first orders and inverse transformation back to the spatial domain, an image without the undesired reference grating, Fig. 2(c, ii), is reconstructed. Next, the Moiré Interferogram is divided into three main sections, separately comprising the two tilting side panels of the Kirigami structure (Sections 1, 2) and one additional section along the center of the structure, partially encompassing the two panels together with the region limited by the vertical cuts. This subdivision process responds to the need to discard the cuts (i.e., discontinuities in the Moiré signals), and leverages the relative nature of the displacements obtained via SM and the confinement of the fringes to the panels. The signals from each section (I_0) are filtered using a Linear Finite Impulse Response Filter (LFIR filter), and subsequently digitally shifted in the frequency domain to obtain three additional signals ($I_{\pi/2}$, I_π and $I_{3\pi/2}$); a process known as Digital Phase Stepping, in contrast to the mechanical analogue where images are shifted by translation of the reference grating [24]. Finally, the wrapped phase (ψ_w) of the signal (i.e., the variable containing the displacement information) is calculated from the four signals, viz. [24]:

$$\psi_w = \tan^{-1}\left(\frac{I_{3\pi/2} - I_{\pi/2}}{I_\pi - I_0}\right) \tag{2}$$

The retrieved phase, in wrapped form, Fig. 2(c, iii), is two-dimensionally unwrapped by first performing a one-dimensional unwrapping along one coordinate, followed by another one-dimensional unwrapping procedure along the other coordinate direction. While a variety of two-dimensional unwrapping procedures are available, with varying degrees of complexity, the described procedure (albeit the simplest method) is able to reconstruct the deformed shape of the Kirigami programmable structures to an acceptable degree. With the unwrapped phase (ψ_{uw}), the relative displacements of three sections can be obtained, viz. [24]:

$$w = \psi_{uw}\left(\frac{p}{2\pi}\right)\frac{1}{K} \tag{3}$$

The obtained three-dimensional surfaces from the above sections are subsequently fitted with two-dimensional polynomials, and the surfaces from the panels are offset by displacement matching with the middle region to retrieve the continuous deformed shape of the tilting panels of the Kirigami, Fig. 2(c, iv-v). The zero displacement is chosen at the centroid of the Kirigami.

3. Results and discussion

3.1. Finite element analysis

3.1.1. Effect of hinge asymmetries

First, the effect of asymmetrical hinges with respect to the x-axis is considered (Fig. 3a–e). In these configurations, one of the hinges is kept unchanged, with dimension h_1 as per Table 1; while its opposing hinge, with dimension h_2, is varied at the expense of L_{x2} up to an upper limit of $h_2 = h_1 + L_x$, in increments of $\Delta h_2 = 0.05$ mm. Remarkably, in all examined cases, the two interior panels exhibit pitchfork-type curves, emanating from a single bifurcation point, as illustrated in three representative responses (σ_{xx}/E vs. θ_x, θ_y) in Fig. 3a–c (*Supplementary Movie 1*). The parametric study further reveals the existence of three markedly distinct regions, characterized by varying h_1/h_2 ratios, governing the manifested two-dimensional rotations (Fig. 3e). In the first region, between the upper limit and $h_1/h_2 \approx 0.312$, the structures presents symmetric tilting with respect to the y-axis, with a dominant behavior of θ_y up to $h_1/h_2 \approx 0.221$, where it subsides to θ_x. Unlike the monotonic behavior of θ_x, θ_y attains a local maximum at $h_1/h_2 \approx 0.147$. More interestingly, at $h_1/h_2 \approx 0.312$, the intrinsic behavior of the structures changes from symmetric to asymmetric with respect to the y-axis, marked by a sudden shift in the values θ_x, θ_y at the symmetry breaking threshold. This second region is characterized by a dominant symmetry breaking response with monotonic trends for both θ_x, θ_y up to $h_1/h_2 = 1$.

Next, the effect of y-asymmetric hinges was studied in a similar fashion, with a parametric sweep carried out in increments

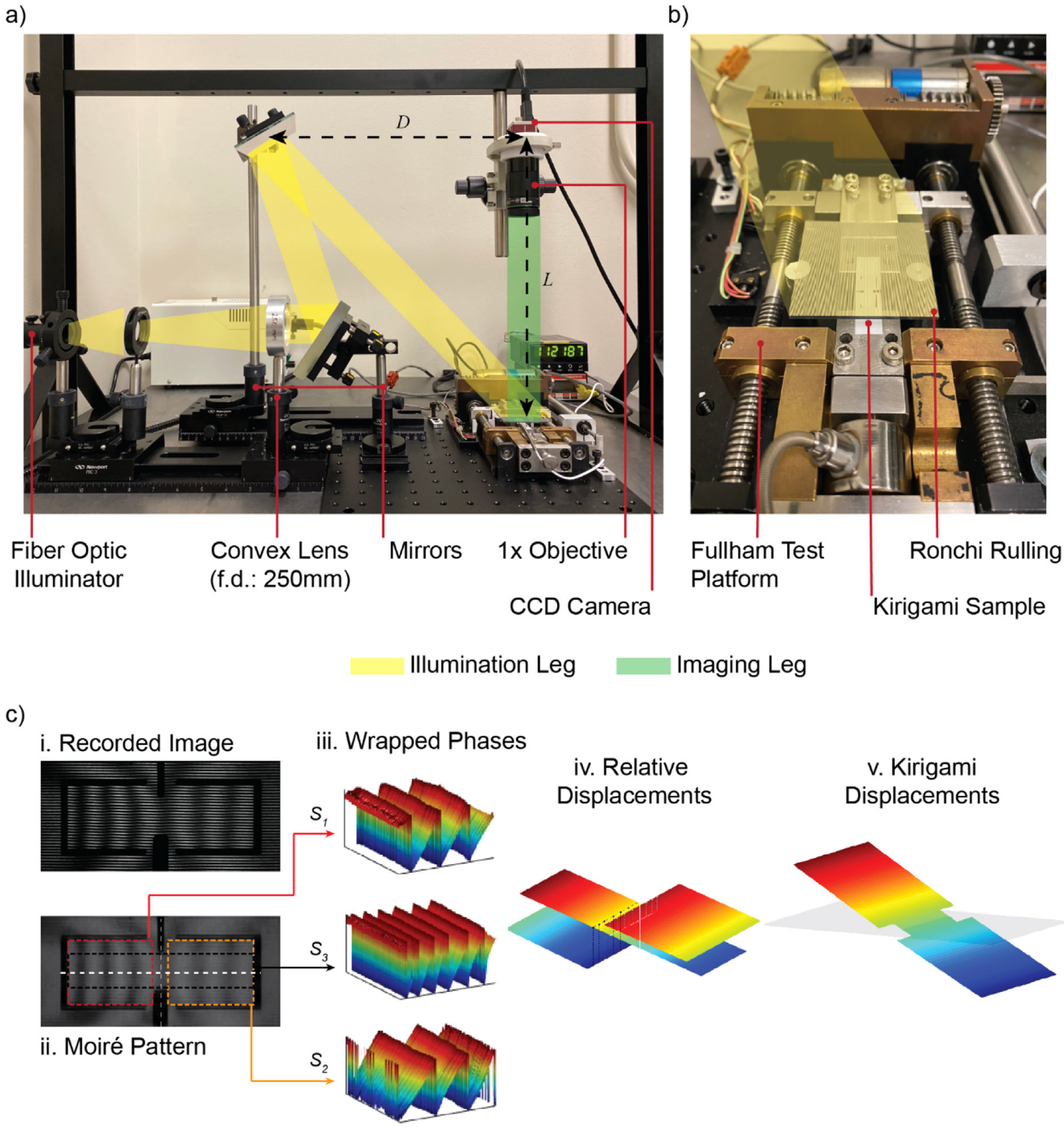

Fig. 2. Shadow Moiré optical and tensile test setup. (a) Front view of experimental setup with main geometric parameters and schematic representation of the light paths for the illumination and imaging legs. (b) Top view of Kirigami specimen mounted on a micro-mechanical test platform and reference grating. (c) Sequence of main steps in shadow Moiré post-processing for the Kirigami.

of $\Delta h_2 = 0.1$ mm. Unlike the previous case, the present hinge configuration precludes two-dimensional tilting, with each panel tilting solely around the y-axis ($\theta_y = 0$) with unequal angles (Fig. 3f–h, *Supplementary Movie 2)*. The corresponding structural responses further reveal that these deformations arise from two bifurcations points occurring in sequence, each one corresponding to each panel. The reason for this behavior lies in the difference in hinge sizes, resulting in different rotational stiffnesses, causing the panel with the smaller hinge size to bifurcate first, and the panel with the larger hinge size to bifurcate at a higher load/displacement. Notably, the overall behavior of the structure is consistent in that it presents symmetry breaking throughout the range of investigated parameters (Fig. 3j). The parametric sweep further reveals that as the ratio gets closer to $h_1/h_2 = 1$, both angles get closer to each other in terms of absolute values, while reducing the effect of sequential bifurcation, until convergence to an equal value, at $h_1 = h_2$. Moreover, the existence of a lower bound is revealed, from which the second angle bifurcates at a hinge ratio of $h_1/h_2 \approx 0.238$. This bound is attributed to the displacement amplitude used in the FEA, since an enlarged stiffness requires a higher load, and consequently, a higher prescribed displacement, to elicit the second bifurcation.

Finally, the combined effect of hinges, asymmetrical with respect to both x-y axes, was parametrically studied in increments of $\Delta h_2 = 0.1$ mm. Similar to the first configuration, these structures display two-dimensional tilting (θ_x, θ_y) from a single bifurcation point (Fig. 4a–c, *Supplementary Movie 3*), with a lower bound at $h_1/h_2 \approx 0.128$ and three distinct regions, along with a symmetry breaking threshold at $h_1/h_2 \approx 0.384$ (Fig. 4e). This last value is slightly higher than the one encountered for the

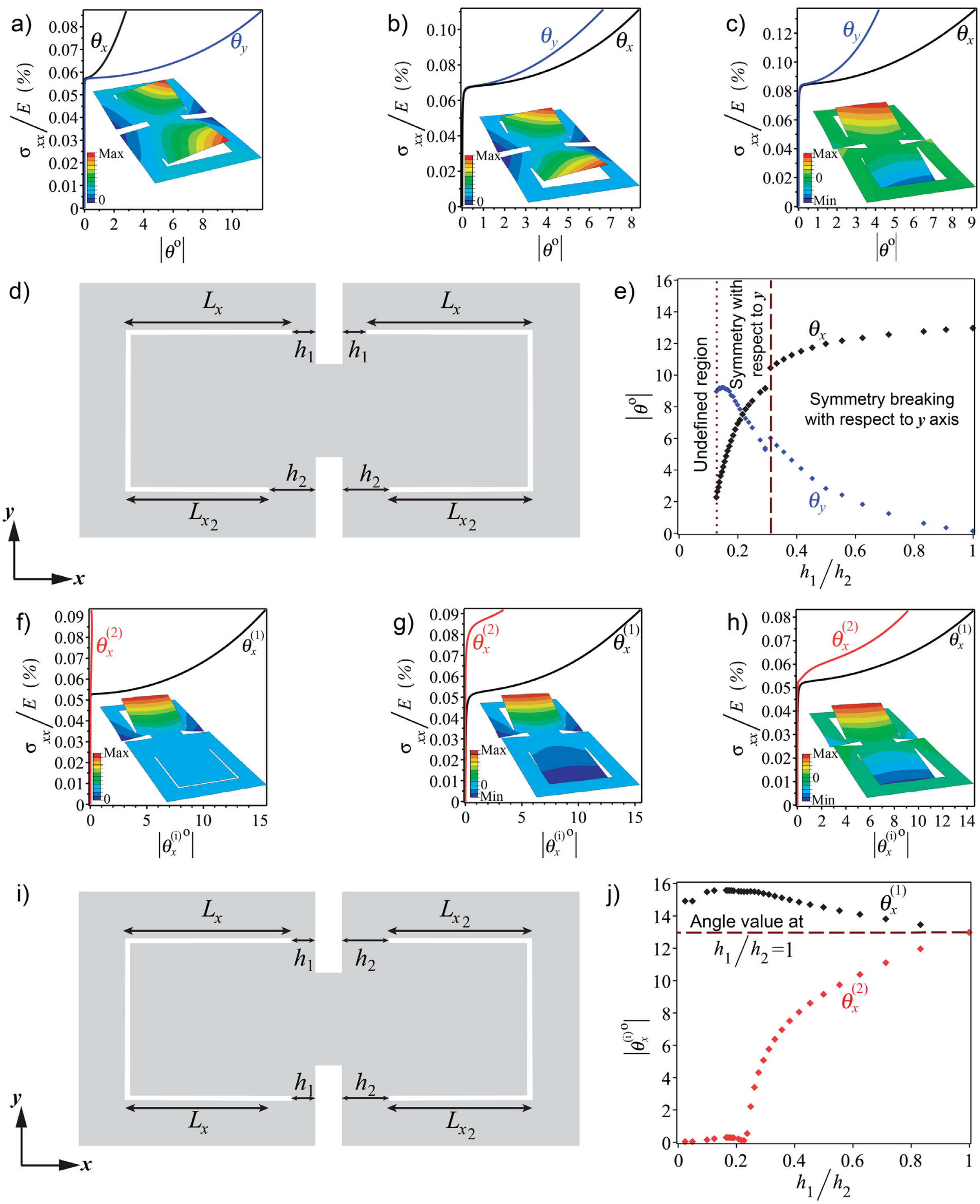

Fig. 3. (a–e) x-asymmetric Kirigami. Non-dimensional equilibrium responses and final out-of-plane displacement contours: (a) $h_1/h_2 = 0.151$; (b) $h_1/h_2 = 0.25$; (c) $h_1/h_2 = 0.5$; corresponding to configuration (d); (e) Rotations versus hinge ratio for $\Delta x/d = 1$, with undefined, y-symmetric (x-asymmetric), and symmetry breaking regions. (f–j) y-asymmetric Kirigami. Non-dimensional equilibrium responses and final out-of-plane displacement contours: (f) $h_1/h_2 = 0.227$, (g) $h_1/h_2 = 0.263$, (h) $h_1/h_2 = 0.5$, corresponding to configuration (i). (j) Rotations versus hinge ratio for $\Delta x/d = 1$. Note: rotations are given in absolute values due to the stochastic nature of the direction of the tilts.

first configuration. In addition, θ_x sees an increase in value with rising hinge ratio, while θ_y sees a maximum value at $h_1/h_2 \approx 0.2$ followed by a decrease, until the two angles meet at $h_1/h_2 \approx 0.233$. As for the symmetry breaking threshold, an abrupt "jump" in values occurs for both angles, until θ_y decreases and vanishes at $h_1/h_2 = 1$. Regarding θ_y values, this configuration presents lower values when compared to the first configuration, showing that the additional asymmetry can interfere with two-dimensional tilting, while slightly increasing the operational range of the symmetric region.

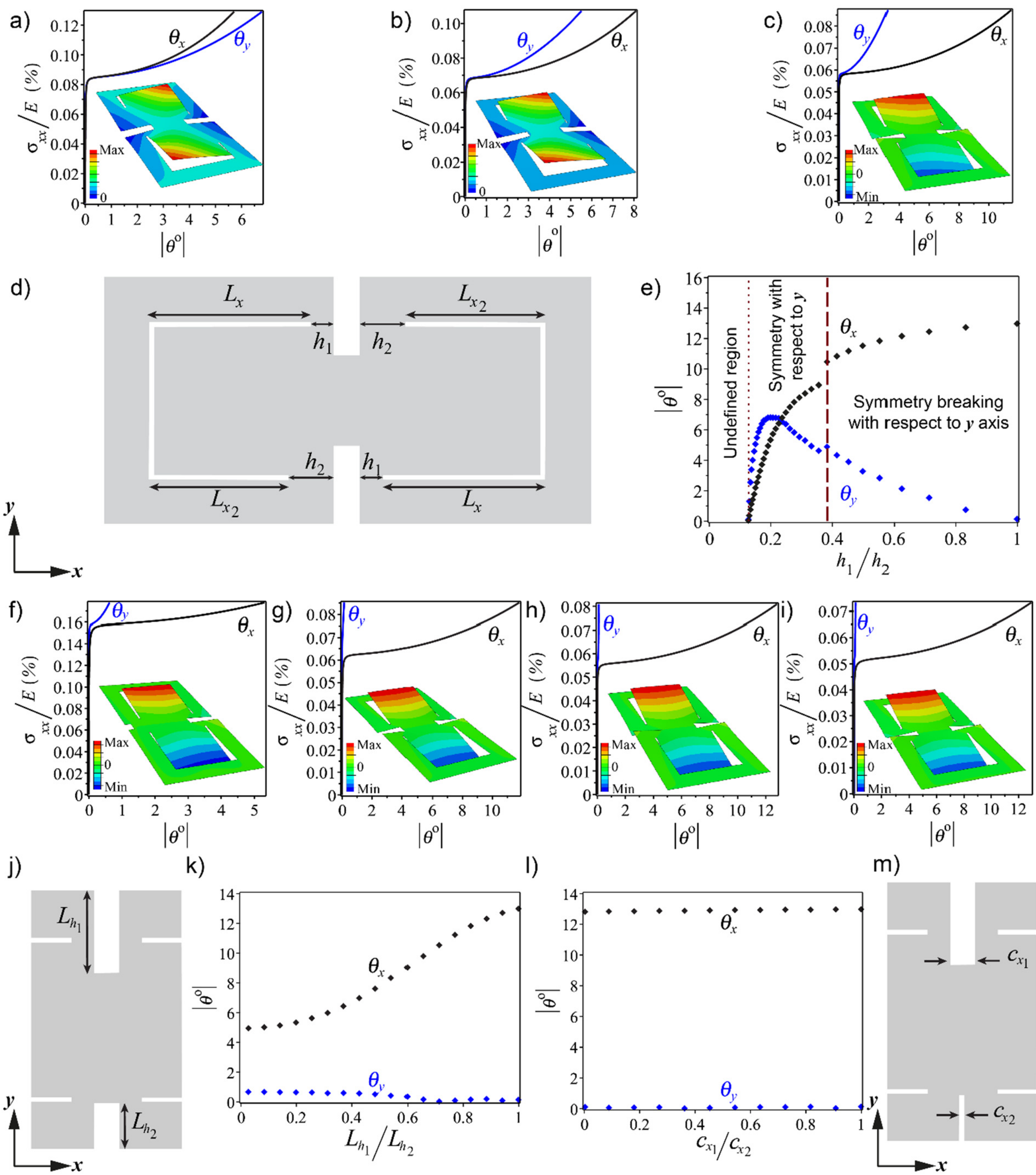

Fig. 4. (a–e) Kirigami with xy-Asymmetry. Non-dimensional equilibrium responses and final out-of-plane displacement contours: (a) $h_1/h_2 = 0.208$; (b) $h_1/h_2 = 0.294$; and (c) $h_1/h_2 = 0.5$; corresponding to configuration shown in (d); (e) Rotations versus hinge ratio for $\Delta x/d = 1$, with undefined, y-symmetric (x-asymmetric), and symmetry breaking regions. (f–g,j–k) Kirigami with asymmetrical cut lengths. Non-dimensional equilibrium responses and final out-of-plane displacement contours: (f) $L_{h_1}/L_{h_2} = 0.2$; (g) $L_{h_1}/L_{h_2} = 0.828$ corresponding to configuration (j); (k) Rotation versus cut length ratio. (h–i,l–m) Kirigami with asymmetrical cut widths. Non-dimensional equilibrium responses and final out-of-plane displacement contours: (j) $c_{x1}/c_{x2} = 0.004$; (k) $c_{x1}/c_{x2} = 0.818$, corresponding to the configuration (l); (m) Rotation versus cut width ratio. Note: Rotations are given in absolute values due to the stochastic nature of the direction of the tilts.

3.1.2. Effect of vertical cuts asymmetries

The last two studied configurations examine the effect of asymmetrical cut lengths (Fig. 4f–g, j–k) and asymmetrical cut widths (Fig. 4h–i, l–m), with overall behavior trends obtained from parametric sweeps, using increments of $\Delta L_{h_2} = \Delta c_{x2} = 0.01$ mm. For both cases, it is revealed that two-dimensional tilting is significantly restricted, with the apparent values of θ_y being relatively negligible in comparison to the values of θ_x. As for the latter angle, variations in cut length can affect its final value, whereas variations in cut width seem to exert no apparent influence. Differences aside, both configurations exhibit a dominant asymmetric behavior throughout the considered parametric range.

3.1.3. Programmable direction via imperfection control

Underlying the deformation modes presented in Figs. 3–4 lies the question whether the direction of the out-of-plane displacements (e.g., Up–Down) can be pre-programmed into the structures without alteration of the motif, and without relying on more complex sources of imperfections (e.g., those arising from residual stresses after the cutting process). Relevant for individual Kirigami structures, the posed question bears relevance when unit Kirigami are integrated into metastructures, where interactions between different unit cells may arise, imposing new interactions and constraints on the system, and potentially hindering the desired excitation of modes apparent at the single Kirigami level. Hence, this degree of control is paramount for a successful application of Kirigami structures in reliable engineering devices.

To gain insight into the possibility of controlling the directions of the tilting panels, the role of surface offsets as imperfections was investigated in Kirigami unit cells, 1D arrays and 3D arrays. The methodology outlined in Section 2.1 for nonlinear FEA was maintained, with the exception that nodes in prescribed panels were perturbed in the out-of-plane direction, as opposed to using specific buckling modes as geometric imperfections. The proposed class of imperfections can be achieved in 3D printing and photolithography techniques without compromising the 2D layout of the Kirigami.

Fig. 5 illustrates the successful direction pre-programming in a variety of Kirigami 1D arrays and in a 3D Kirigami tube with deployable panels. In the 1D metastructures, y-asymmetric and xy-asymmetric Kirigami cells were concatenated in a 6×1 array and subject to tension, following the imperfection pattern shown in Fig. 5a. The tilt of the y-asymmetric structures was pre-programmed to yield continual (3 Up–3 Down) and alternate (Up–Down x3) out-of-plane modes. Conversely, the nature of the displacement modes discovered for the xy-asymmetric Kirigami enabled tailoring the individual panel imperfections to yield a mixed sequence (Up/Up–Down/Down–Up/Down: Symmetric). At the 3D level, perhaps more interesting is the fact that in the tube made of y-asymmetric Kirigami, no imperfections are required to tilt the panels, hence a natural emergence of the Kirigami effect is predicted due to the Poisson effect (Fig. 5b,i). To enforce outward tilts, two different levels of imperfection are studied. At the first level, panels continue to tilt inwards, despite having the same imperfections that were successful in pre-programming deformation in 1D arrays. At a higher level of imperfections, the desired displacement is predicted. Though simple, these toy models underscore the importance and challenges that Kirigami metastructures pose to yield robust functional structures.

3.2. Experimental validation via Shadow Moiré

Recorded SM interferograms and the reconstructed three-dimensional shapes from the selected cases tested are shown in Fig. 6a–f. Reconstructed surfaces are in very good agreement with the programmable shapes predicted by the FEA. Particularly interesting are the results shown in Fig. 6e, where the xy-asymmetric structure is shown to display asymmetric out-of-plane deformation (i.e., one panel up, one panel down), as predicted by imperfection analysis, and stressing both the importance of initial geometric imperfections and the potential to control the deformation modes. Experimental validation of the predicted shapes highlights the scalability of these designs, which have been shown to work at the nanoscale [8], hence encompassing four orders of magnitude.

3.3. Potential applications

The variety of programmable shapes, enabled by simple variations of the proposed two-dimensional Kirigami, promise to influence several applications in diverse fields encompassing optics, acoustics, energy harvesting and space exploration, as well as fluid and thermal-flow control. In addition to the available shape-space, applications of these programmable Kirigami benefit from the simplicity of their cut-layout, stretch-actuation modes, and their ability to control the deformation via imperfection engineering. Access to the bifurcated states with smooth transitions further enables force–displacement control, a pivotal requirement in sensitive applications.

3.3.1. Light modulation: from energy harvesting to solar sails

The realm of optics and light-steering technologies, coupled with energy harvesting, constitute a particularly fertile ground for the implementation of shape programmable Kirigami acting at scales encompassing the nano-, micro- and macroscale. Perhaps the most obvious applications of these Kirigami structures are in the form of multiform mirrors, programmable thin lenses and diffractive elements, which can compete with current MEMS based methods, especially when dealing with mirror arrays. Presently, such paradigms require actuation signals for each mirror, increasing the overall level of engineering and complexity in design and follow-up fabrication [27,28]. Although recent progress towards design of 2D arrays of deformable plates has been achieved, actuation can still be cumbersome due to the required circuitry [29]. In sharp contrast, the value of the variegated shapes reported here, lies both in their ability to be easily incorporated into larger arrays and their conformity to predetermined shapes upon simple stretch actuation, thus greatly simplifying the design to a single actuation source at the edges of the metastructure.

The scalable nature of these Kirigami designs [8], makes said advantages non-exclusive to the micro scale, which makes them promising candidates for solar collection applications, where tracking solar troughs and panels are commonly employed to reflect and absorb sunlight, respectively. Current paradigms rely on actuation and control of heavy rotating panel rows [30], individual mirrors to create linear Fresnel reflectors [31], or Kirigami stretchable strips able to unidirectionally reflect light [7,18]. The Kirigami designs presented here, not only have higher usable areas (versus Kirigami strips) and adaptive control via simple stretching, but can also achieve two-dimensional tilting, which could significantly expand the versatility of such systems.

The discovered y-Asymmetric Kirigami for example, could be assembled into linear arrays and used as multimodal solar collectors for dual solar energy harvesting, taking advantage of the latest developments in solar harvesting flexible thin films [32]. The tilting panels could form Fresnel mirrors with stretch based variable focal distances (*Supplementary Movie 4*), whereas the still panels and frames could be used as solar panels for direct solar collection. With the aid of ray tracing simulations performed in COMSOL Multiphysics, eight Kirigami geometries ($n = 8$) were selected and placed at a constant separation distance ($s = 12.55$ mm), and actuated so that the angle of each panel (θ_i) enables focusing of light (focal distance $h_f = 70$ mm) incoming at a vertical angle ($\theta_s = 0^\circ$), as per [33] and demonstrated in Fig. 7(a).

Furthermore, the identified Kirigami shapes could be engineered as optical or acoustic diffusers to create tailored spatial distributions of light and sound, operating on reflection principles. For example, an array of six x-asymmetric Kirigami reflective structures was used in a ray tracing simulation with collimated light shone from above. Upon stretching, the distribution of reflected light is dramatically altered, while still maintaining an ordered distribution, Fig. 7(b). Extension of these concepts could be used to impact the energetic efficiency of illumination or sound systems in interactive displays or even in stealth technologies, where it has been shown that rough topographies can effectively conceal targets in radar-type sensing [34].

Conversely, instead of using the Kirigami structures to direct light, light could be exploited to steer solar-sail type structures

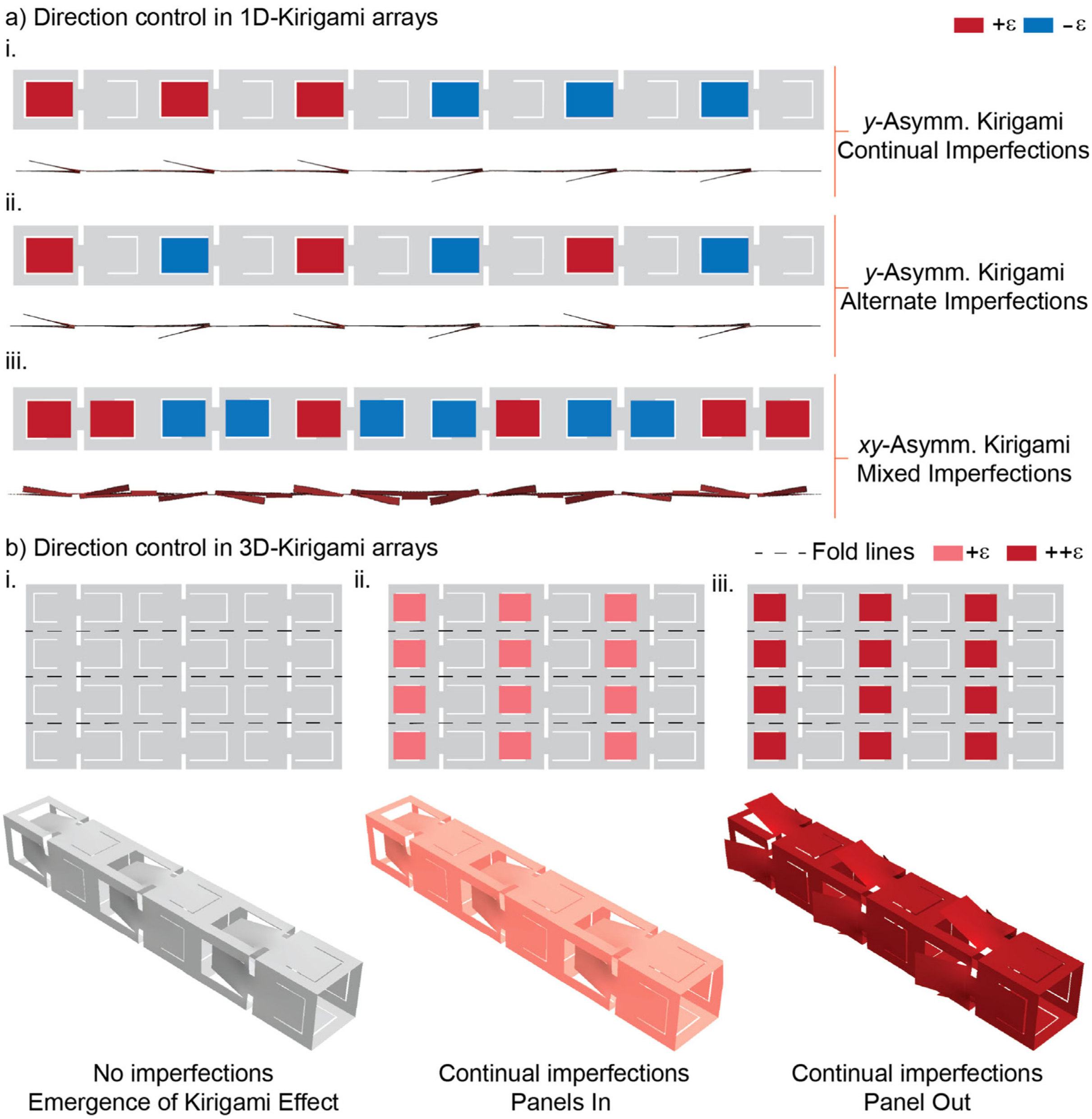

Fig. 5. Response of multidimensional Kirigami arrays due to pre-programmed imperfections. (a) 1D Kirigami arrays: (i–ii) *y*-asymmetrical Kirigami array with continual and alternating imperfections; (iii) *xy*-asymmetrical Kirigami with mixed imperfections. (b) 3D Kirigami arrays: (i) No imperfections, panels in (ii) Continual outwards imperfections, panels in; (iii) Continual outwards imperfection, panels out.

comprised of a multitude of shape programmable Kirigami reflectors. Kirigami with the investigated cut-layout have high surface area-to-mass ratios, structural rigidity, and due to their shape-programmable nature, the ability to actively modify the Solar Radiation Pressure force vector, which in the case of flat plates is a function of the surface orientation ($\boldsymbol{n}$) and reflectivity [35]. As such, manufacturing of shape programmable Kirigami, combined with optically responsive materials (e.g., thermochromic materials), could open a gamut of linear and angular steering control possibilities in deployable solar sails and microsatellites, Fig. 7(c).

3.3.2. Other applications

The integration of Kirigami structures into morphable surfaces also holds the potential to be exploited in friction and hydro-/aerodynamic flow control applications. Unlike previous attempts at friction and adhesion control relying on still configurations [36], Kirigami structures resembling placoid scales have been shown to allow active modulation of dry friction [37]. The various Kirigami shapes here presented could also be used for active modulation of dry friction with the added benefit of simpler cut-layouts. Furthermore, by tailoring the assembly of many various Kirigami cells, higher-order shapes could be achieved (e.g., mountain-valley, Fig. 7d,i), thus enabling hierarchical and multiscale friction modulation. Moreover, the possibility of controlling the imperfections to favor a specific tilt direction, coupled with the range of observed curvatures and nonlinear structural responses, could be integrated in haptic feedback systems for various texture sensing applications.

Additionally, surface patterning via stretch actuation could be used in flow control systems to actively modify fluid–solid boundaries and impact heat transfer. For instance, certain Kirigami configurations yield shapes resembling the dermal denticles found in the skins of sharks, which have been shown to reduce pressure drag and improve hydrodynamic performance

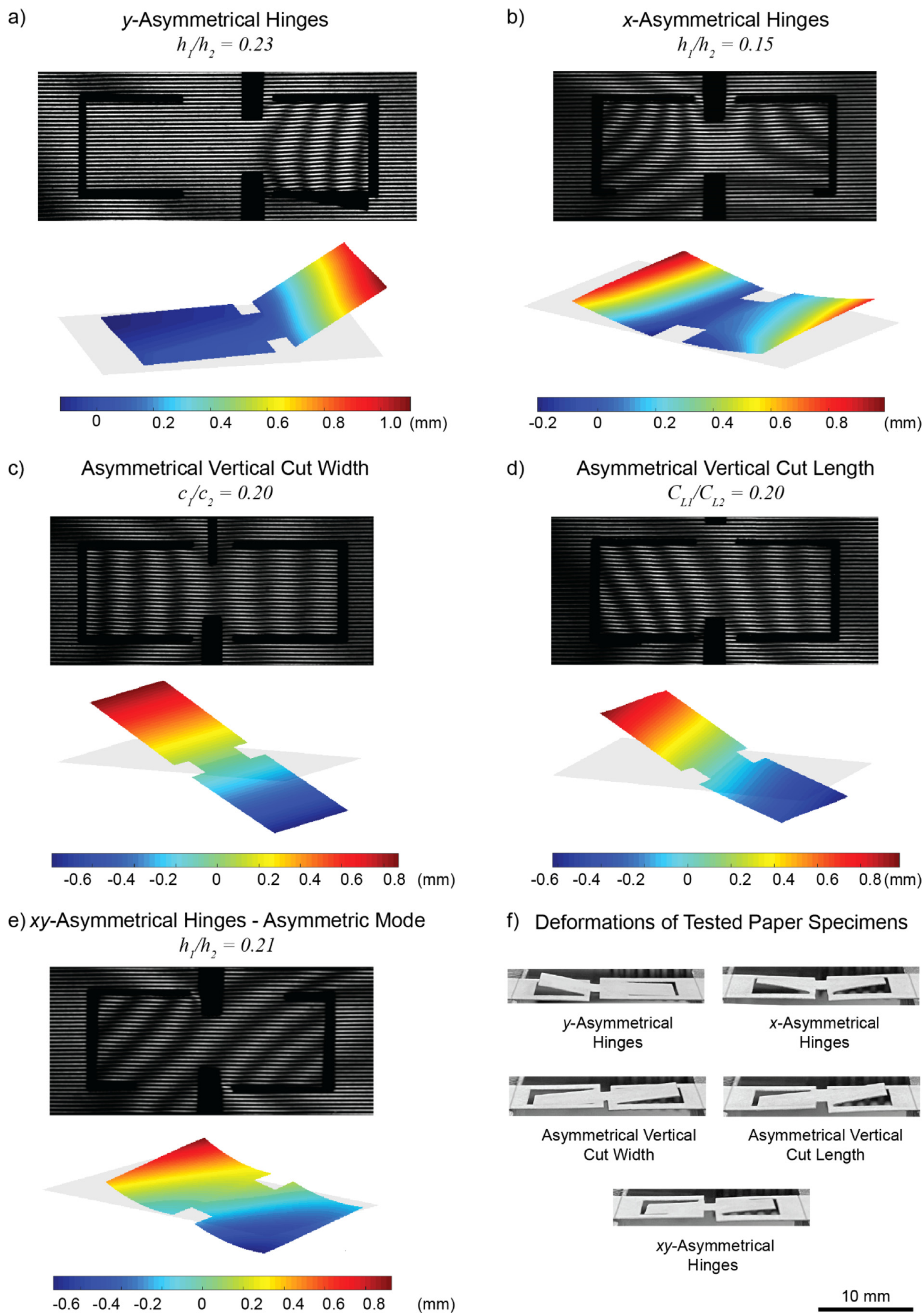

Fig. 6. Experimental validation via SM technique. Interferograms and reconstructed deformed shapes. (a) y-axis asymmetrical hinges $h_1/h_2 \approx 0.23$; (b) x-axis asymmetrical hinges, $h_1/h_2 \approx 0.15$; (c) Asymmetrical vertical cut width $c_{x1}/c_{x2} \approx 0.2$; (d) Asymmetrical vertical cut length $L_{h_1}/L_{h_2} \approx 0.2$; (e) $xy-$ axes asymmetrical hinges , $h_1/h_2 \approx 0.21$, asymmetric deformation mode; (f) Side view of tested paper samples.

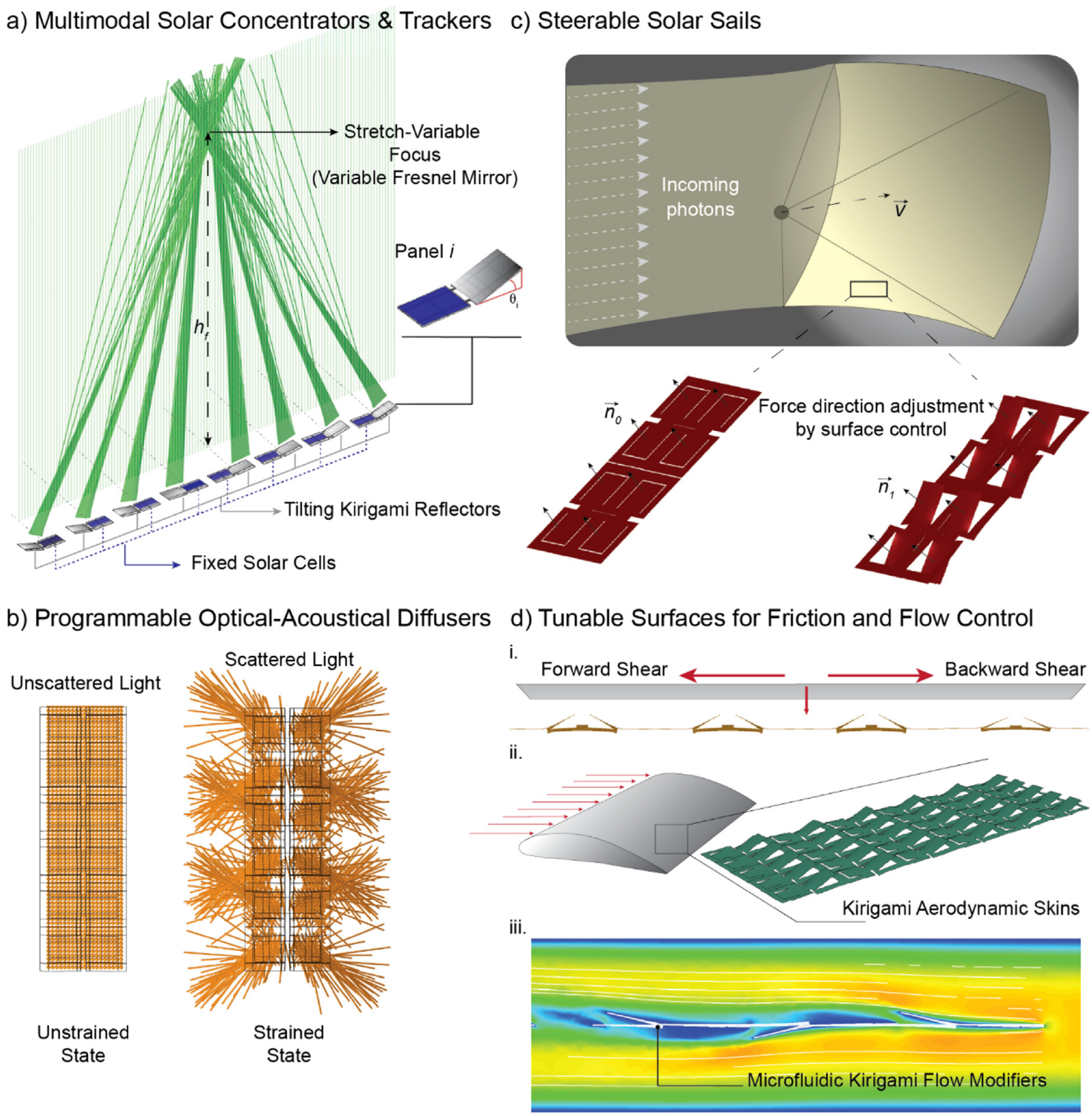

Fig. 7. Potential applications of shape programmable Kirigami structures. (a) Ray tracing simulations of a Linear Fresnel mirror comprised of *y*-asymmetric Kirigami; (b) Ray tracing simulations of optical reflective diffusers made of *x*-asymmetric Kirigami; (c) Conceptual Kirigami solar sails with steering control via adaptive shape-morphing; (d) Conceptual applications of Kirigami for friction (i) and fluid flow control (ii) and velocity profile obtained via Computational Fluid Dynamics of water around Kirigami flow modifiers (iii).

via passive bristling mechanisms [38]. Hydrodynamic and aerodynamic skins, as well as smart fabrics, could incorporate programmable Kirigami structures to actively emulate such flow modifying mechanisms and implemented along sections of aircraft fuselage or ship hulls, Fig. 7(d, ii). Similarly, Kirigami arrays could be employed as inserts for active modulation of heat transfer and fluid mixing in microfluidic applications. Existing solutions in the form of winglets and twisted-tapes have been proven to affect heat transfer, but in passive form [39]. Depending on their deformation state, the Kirigami structures discussed here could act as tunable vortex generators to perturb the flow field and affect the evolution of the boundary layer, to impact heat transfer rate, Fig. 7(d, iii).

4. Summary and conclusions

Investigations on the effects of asymmetries in the hinges and cuts of a simple Kirigami motif illustrate the rich space of achievable 3D out-of-plane morphologies. Depending on the Kirigami cut dimensions, a range of three-dimensional surfaces can be obtained, exhibiting one- and two-dimensional rotations with symmetry breaking characteristics. Access to these deformed states was found to be facilitated by double pitchfork buckling phenomena, emanating from single bifurcations, or double sequential bifurcation points, as identified by rigorous FEA parametric studies and experimental measurements using shadow Moiré.

The undertaken analyses also provide insight in the form of design guidelines for the application of the Kirigami motif into a variety of engineering structures. For example, should two-dimensional tilting be a desirable outcome, one could include asymmetries with respect to the longitudinal axis of the Kirigami motif or a combination of asymmetries with respect to the longitudinal and transverse axes. If, on the other hand, gradual changes are sought, where each interior panel attains a different angle around the longitudinal axis, asymmetries with respect to the transverse axis should be employed. Conversely, variations in cut widths and lengths furnish insensitivity in terms of achievable angles and participating modes, respectively. Such distinctions are of value in determining the degree of imperfections needed for a given application. The studied Kirigami pattern, though simple at first glance, exhibits a versatility that, if bolstered by machine learning and optimization techniques, could be leveraged to design a cornucopia of multiscale applications, forming the basis for application-driven research.

The successful experimental validation of computational predictions, using a different material and scaled geometry, demonstrate scalability and transferability of the Kirigami design principles. As such, the observed behaviors could be leveraged with 2D and active matter. For example, a tunable electromagnetic field could be achieved, in the subwavelength regime, using 2D materials. In the context of active material, e.g., cell cultures, the 3D morphing could be exploited in the investigation of curvotaxis on cellular migration and tissue assembly. Regardless of scale, material and application, Kirigami metastructures and the potential emergence of novel effects from their assembly posit intriguing open questions, currently under vigorous investigation by various groups.

CRediT authorship contribution statement

Nicolas A. Alderete: Conceptualization, Experimentation, Data analysis, Writing. **Lior Medina:** Conceptualization, Numerical simulations, Data analysis, Writing. **Luciano Lamberti:** Shadow Moire software, Data analysis, Editing. **Cesar Sciammarella:** Shadow Moire sofware, Data analysis, Editing. **Horacio D. Espinosa:** Conceptualization, Methodology, Data interpretation, Editing, Project coordination.

Declaration of competing interest

The authors declare that they have no known competing financial interests or personal relationships that could have appeared to influence the work reported in this paper.

Acknowledgments

H.D.E. acknowledges the support of the AFOSR through Award # FA9550-20-1-0258 and the NSF through award # CMMI-1953806. L.M. acknowledges the support of the Tel Aviv University — Northwestern University joint postdoctoral fellowship. N.A.A. and H.D.E. gratefully acknowledge financial support from the Roberto Rocca Education Program (RREP), Argentina. This work made use of the laser cutting facilities available at the Ford Shop, Segal Design Institute at Northwestern University.

Appendix A. Supplementary data

Supplementary material related to this article can be found online at https://doi.org/10.1016/j.eml.2020.101146.

References

[1] M.K. Blees, A.W. Barnard, P.A. Rose, S.P. Roberts, K.L. McGill, P.Y. Huang, A.R. Ruyack, J.W. Kevek, B. Kobrin, D.A. Muller, P.L. McEuen, Nature 524 (2015) 204.
[2] W. Zheng, W.C. Huang, F. Gao, H.H. Yang, M.J. Dai, G.B. Liu, B. Yang, J. Zhang, Y.Q. Fu, X.S. Chen, Y.F. Qiu, D.C. Jia, Y. Zhou, P.A. Hu, Chem. Mater. 30 (2018) 6063.
[3] M.A. Dias, M.P. McCarron, D. Rayneau-Kirkhope, P.Z. Hanakata, D.K. Campbell, H.S. Park, D.P. Holmes, Soft Matter 13 (2017) 9087.
[4] G.P.T. Choi, L.H. Dudte, L. Mahadevan, Nature Mater. 18 (2019) 999.
[5] A. Rafsanjani, D. Pasini, Extreme Mech. Lett. 9 (2016) 291.
[6] A. Rafsanjani, K. Bertoldi, Phys. Rev. Lett. 118 (2017).
[7] W. Wang, C. Li, H. Rodrigue, F.P. Yuan, M.W. Han, M. Cho, S.H. Ahn, Adv. Funct. Mater. 27 (2017).
[8] X. Zhang, L. Medina, H. Cai, V. Aksyuk, D. Lopez, H. Espinosa, Kirigami engineering-nanoscale structures exhibiting a range of controllable 3D configurations, Adv. Mater. (2020) http://dx.doi.org/10.1002/adma.202005275.
[9] K. Das, R.C. Batra, Smart Mater. Struct. 18 (2009).
[10] L. Medina, R. Gilat, S. Krylov, Internat. J. Engrg. Sci. 130 (2018) 75.
[11] G.J. Simitses, D.H. Hodges, Fundamentals of Structural Stability, Elsevier/Butterworth-Heinemann, Amsterdam ; Boston, 2006.
[12] N. Hu, R. Burgueno, Smart Mater. Struct. 24 (2015).
[13] M. Pishvar, R.L. Harne, Adv. Sci. (2020).
[14] K. Yong, S. De, E.Y. Hsieh, J. Leem, N.R. Aluru, S. Nam, Mater. Today 34 (2020) 58.
[15] J. Rossiter, S. Sareh, Kirigami Design and Fabrication for Biomimetic Robotics, SPIE, 2014.
[16] J. Rossiter, S. Sareh, Proc. SPIE 9055 (2014).
[17] L.Z. Xu, X.Z. Wang, Y. Kim, T.C. Shyu, J. Lyu, N.A. Kotov, ACS Nano 10 (2016) 6156.
[18] A. Lamoureux, K. Lee, M. Shlian, S.R. Forrest, M. Shtein, Nature Commun. 6 (2015).
[19] D. Systèmes, Abaqus 6.13 Online Documentation, Providence, RI, USA, 2013.
[20] F. Bloom, D. Coffin, Handbook of Thin Plate Buckling and Postbuckling, Chapman & Hall/CRC, Boca Raton, FL, 2000.
[21] S. Timoshenko, J.M. Gere, Theory of Elastic Stability, second ed., Dover Publications, Mineola N.Y, 2009.
[22] S.J.P. Callens, A.A. Zadpoor, Mater. Today 21 (241) (2018).
[23] G.L. Cloud, Optical Methods of Engineering Analysis, Cambridge University Press, Cambridge; New York, 1995.
[24] C.A. Sciammarella, F.M. Sciammarella, Experimental Mechanics of Solids, Wiley, Chichester, West Sussex, U.K, 2012.
[25] D. Post, B. Han, P. Ifju, High Sensitivity Moiré: Experimental Analysis for Mechanics and Materials, Springer-Verlag, New York, 1994.
[26] Springer Handbook of Experimental Solid Mechanics, Springer, Berlin, 2008.
[27] V.A. Aksyuk, M.E. Simon, F. Pardo, S. Arney, D. Lopez, A. Villanueva, In Optical MEMS design for telecommunications applications, Solid-state sensor, actuator and Microsystems workshop, Hilton Head Island, South Carolina, 2002, 1.
[28] A. Crunteanu, D. Bouyge, D. Sabourdy, P. Blondy, V. Couderc, L. Grossard, P.H. Pioger, A. Barthelemy, J. Opt. A-Pure Appl. Opt. 8 (2006) S347.
[29] A. Uno, Y. Hirai, O. Tabata, T. Tsuchiya, Proc. IEEE Microsyst. Electron. (2018) 704.
[30] K. Vyas, Guide for Solar Tracking System Design & Development of Prototype for SPV Tracking System, LAP LAMBERT Academic Publishing, 2017.
[31] H.A. S. Pellegrino, S.A. Hajimiri, M. Arya, C. Leclerc, N. Lee,
[32] S.A. Hashemi, S. Ramakrishna, A.G. Aberle, Energy Environ. Sci. 13 (2020) 685.
[33] Y.Q. Zhu, J.F. Shi, Y.J. Li, L.L. Wang, Q.Z. Huang, G. Xu, Energy Convers. Manage. 146 (2017) 174.
[34] E.L. Clare, M.W. Holderied, Elife 4 (2015).
[35] M.P. Lorraine Weis, Active Solar Sail Designs for Chip-Scale Spacecraft. in: 28th Annual AAIA/USU Conference on Small Satellites, Logan, Utah, 2014.
[36] J. Seo, J. Eisenhaure, S. Kim, Extreme Mech. Lett. 9 (2016) 207.
[37] S. Babaee, S. Pajovic, A. Rafsanjani, Y.C. Shi, K. Bertoldi, G. Traverso, Nat. Biomed. Eng. (2020).
[38] S.P. Devey, A.W. Lang, J.P. Hubner, J.A. Morris, M.L. Habeggar, Experimental analysis of passive bristling in air to enable mako-shark-inspired separation control, in: AIAA AVIATION 2020 FORUM, 2020.
[39] S. Rashidi, M. Eskandarian, O. Mahian, S. Poncet, Therm. Anal. Calorim. J. 135 (2019) 437.